Chapter 3

Robust Damping Control for Integrated Wind Turbine Power Networks During Low Inertia Condition

3.1 Introduction

This chapter presents a modal analysis-based impact analysis of the change in system inertia due to the integration of the large-scale Doubly Fed Induction Generator (DFIG)-based Wind Turbine System (WTS) on the power system damping in inter-area oscillation modes. The impact of replacement of a synchronous generator by WTS of same MVA capacity on system dynamics, such as emergence of new critical modes of inter-area oscillations affecting system stability is studied. Further, a double-channel H_∞ scheme based Wide-Area Damping Controller (WADC) is proposed for WTS, which provides sufficient damping of prominent oscillation modes and enhanced stability margin to alleviate the negative impact of reduction in system inertia. The comparative assessment of the proposed controller with a PSS-based WADC on a modified New England ten-machine system validates the performance and is found to be more effective in mitigating inter-area oscillation in the system. The real-time feasibility of the proposed double-channel H_∞ WADC is evaluated on the Real-Time Digital Simulator (RTDS) platform. The simulation results show that the proposed WADC can successfully mitigate various inter-area modes simul-

taneously. Furthermore, it provides robust performance for various contingencies, time delays in feedback signals, and uncertainties associated with different operating scenarios of WTS.

3.2 Modeling of Power System

3.2.1 Modeling of DFIG-based wind turbine system

The general layout of a DFIG-based WTS is shown in Fig. 3.1. The electro-mechanical dynamics are the primary focus of this work since they are used to explore the impact on power system inter-area oscillations as a result of integration of WTS that causes the change in system inertia condition. This Sub-section presents the modelling of DFIG-based WTS.

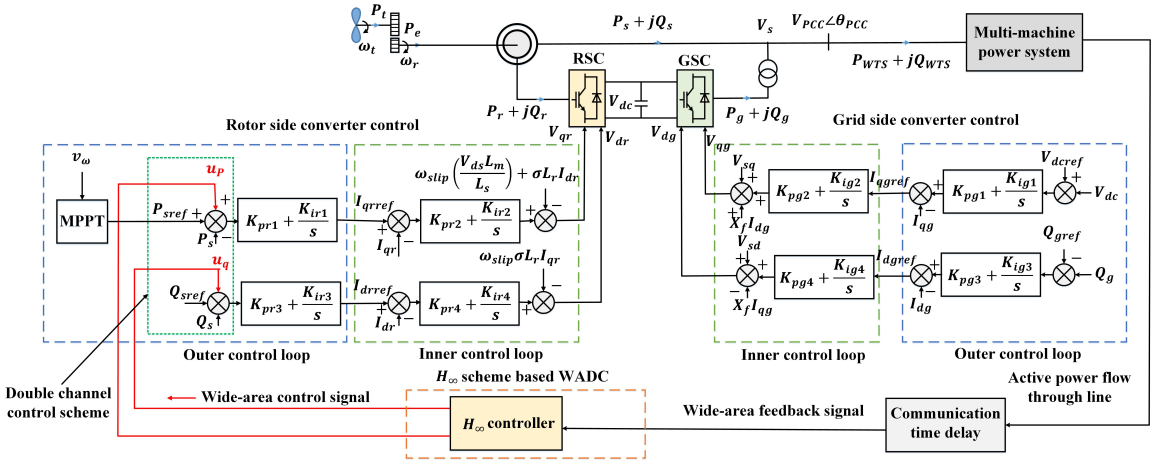

Figure 3.1: DFIG-based WTS configuration and associated control system.

3.2.1.1 Model of drive-train

A two-mass drive train could be used to model the wind turbine, gearbox, generator, and shafts. A two-mass driven system is mathematically explained as [76]:

$$\begin{cases} p\omega_t = \frac{1}{2H_t}\left[T_m + D_{tg}\left(\omega_r - \omega_t\right) - D_t\omega_t - T_g\right] \\ p\omega_r = \frac{1}{2H_g}\left[D_{tg}\left(\omega_t - \omega_r\right) - D_g\omega_r + T_g - T_e\right] \\ pT_g = K_{tg}\omega_e\left[\omega_t - \omega_r\right] \end{cases} \tag{3.1}$$

where, p represents the differential operator; ω_t, ω_r, and ω_e represent the speeds of the wind turbine, generator, and synchronous reference frame, respectively. The inertia

of a wind turbine is H_t. The damping coefficients between the generator and wind turbine, the wind turbine damping coefficient, the drive train shaft stiffness coefficient, and the damping coefficient of the induction generator are represented as D_{tg}, D_t, K_{tg}, and D_g, respectively. The electromagnetic torque of the generator is T_g and wind turbine mechanical torque is T_m, calculated as follows:

$$T_m = \frac{P_m}{\omega_r} = \frac{0.5C_p(\beta,\lambda)R^2v_\omega^3}{\omega_r} \tag{3.2}$$

where β , λ, C_p , R, ρ, v_w, and P_m are the wind turbine pitch angle, tip speed ratio, power coefficient of the blade, rotor radius, air density, wind speed, and mechanical power, respectively.

3.2.1.2 Induction generator model

The voltage equations of the induction machine can be expressed in dq reference frame as follows [77].

$$\begin{cases} p\psi_{qs} = \omega_b\left[V_{qs} - \frac{r_s x'_{rr}}{\Omega}\psi_{\mathrm{qs}} - \frac{\omega}{\omega_b}\psi_{ds} + \frac{r_s x_m}{\Omega}\psi'_{qr}\right] \\ p\psi_{ds} = \omega_b\left[V_{ds} - \frac{r_s x'_{rr}}{\Omega}\psi_{\mathrm{ds}} + \frac{\omega}{\omega_b}\psi_{qs} + \frac{r_s x_m}{\Omega}\psi'_{dr}\right] \\ p\psi'_{qr} = \omega_b\left[V'_{qr} + \frac{r'_r x_m}{\Omega}\psi_{\mathrm{ds}} - \frac{r'_r x_{ss}}{\omega_b}\psi'_{qr} - \frac{(\omega-\omega_r)}{\omega_{\mathrm{b}}}\psi'_{dr}\right] \\ p\psi'_{dr} = \omega_b\left[V'_{dr} + \frac{r'_r x_m}{\Omega}\psi_{\mathrm{ds}} - \frac{r'_r x_{ss}}{\omega_b}\psi'_{dr} + \frac{(\omega-\omega_r)}{\omega_{\mathrm{b}}}\psi'_{qr}\right] \end{cases} \tag{3.3}$$

where, $\Omega = x_{ss}x_{rr'} - x_m^2$, ω_b and ω represent the base angular velocity and the rotational speed of the arbitrary reference frame, respectively; x_m, $x_{rr}^{'}$, $r_r^{'}$, and r_s are the magnetizing reactance, rotor reactance, rotor resistance, and stator resistance of the generator, respectively; ψ_s, $\psi_r^{'}$, V_s, $V_r^{'}$, are the dq-axis component of the stator flux, rotor flux, stator voltage, and rotor voltage, respectively.

3.2.1.3 WTS converter primary controller

The structure of the WTS, along with the associated Rotor Side Converter (RSC) and Grid Side Converter (GSC) primary controller, is shown in Fig. 3.1. The WTS facilitates the independent regulation of reactive and active power through the vector control technique. The q-axis control loop generates the control signal V_{qr} (i.e. q-axis RSC voltage), which effectively regulates the active power output of the WTS. Moreover, the maximum power point tracking algorithm determines the reference active power (P_{sref}) output intended

for the RSC. On the other hand, the d-axis control loop of RSC controls the reactive power output of WTS through control signal V_{dr}(i.e. d-axis RSC voltage). The dq-axis rotor current references (I_{qrref} and I_{drref}) are generated for the RSC inner current control loop as follows:

$$\begin{cases} I_{qrref} = \left(K_{pr1} + \dfrac{K_{ir1}}{s}\right)(P_s - P_{sref} + u_p) \\ I_{drref} = \left(K_{pr3} + \dfrac{K_{ir3}}{s}\right)(Q_s - Q_{sref} + u_q) \end{cases} \tag{3.4}$$

where, P_s, Q_s, and Q_{sref} represent the active power, reactive power, and reference reactive power of the WTS, respectively; u_p and u_q are the wide-area control signal for the active and reactive control loop of the RSC, respectively.

The dq-axis RSC voltages (V_{qr} and V_{dr}) are generated through the inner-current control loop as follows:

$$\begin{cases} V_{qr} = \left(K_{pr2} + \dfrac{K_{ir2}}{s}\right)(I_{qrref} - I_{qr}) + \\ \qquad \omega_{slip}\left(\dfrac{V_{ds}L_m}{L_s}\right) + \sigma L_r I_{dr} \\ V_{dr} = \left(K_{pr4} + \dfrac{K_{ir4}}{s}\right)(I_{drref} - I_{dr}) + \\ \qquad \omega_{slip}\sigma L_r I_{dr} \end{cases} \tag{3.5}$$

where, $\sigma = \dfrac{1 - L_m^2}{L_s L_r}$, and $\omega_{slip} = \dfrac{\omega - \omega_r}{\omega_b}$; L_s, L_r, and L_m are the stator, rotor, magnetizing reactance of induction generator, respectively; I_{dr}, and I_{qr} are the dq-axis rotor current; K_{pr1}, K_{pr3}, K_{ir1}, and K_{ir3} are the proportional and integral gain coefficients of the Proportional plus Integral (PI) controller of RSC outer control loop for active and reactive power control, respectively; K_{pr2}, K_{pr4}, K_{ir2}, and K_{ir4} are the PI controller's proportional and integral gain coefficients of the RSC inner control loop for active and reactive current control, respectively.

The primary objectives of the GSC are to ensure the stability of the DC link voltage and to control the GSC reactive power output. In the case of the GSC, the outer control loop on the q-axis is responsible for regulating the DC link voltage (V_{dc}), while the d-axis control is accountable for adjusting the converter's reactive power (Q_g), as depicted in Fig. 3.1. The generation of dq-axis current references (I_{qgref} and I_{dgref}) for the GSC's inner current control loop are as follows:

$$\begin{cases} I_{qgref} = \left(K_{pg1} + \dfrac{K_{ig1}}{s}\right)(V_{dcref} - V_{dc}) \\ I_{dgref} = \left(K_{pg3} + \dfrac{K_{ig3}}{s}\right)(Q_{gref} - Q_g) \end{cases} \tag{3.6}$$

The dq-axis GSC voltages (V_{qg} and V_{dg}) are generated via the inner-current control loop as follows:

$$\begin{cases} V_{qg} = \left(K_{Pg2} + \dfrac{K_{ig2}}{s}\right)(I_{qgref} - I_{qg}) + \\ \qquad\qquad X_f I_{dg} + V_{sq} \\ V_{dg} = \left(K_{Pg4} + \dfrac{K_{ig4}}{s}\right)(I_{dgref} - I_{dg}) - \\ \qquad\qquad X_f I_{dg} + V_{sd} \end{cases} \tag{3.7}$$

where,V_{dcref} is the reference voltage of the voltage control loop of GSC; Q_{gref} is the reference reactive power of GSC; X_f is the filter reactance; I_{dg}, and I_{qg} are the dq-axis current of GSC; K_{pg1}, K_{pg3}, K_{ig1}, and K_{ig3} are the proportional and integral gain coefficients of the PI controller in the GSC outer control loop, respectively; K_{pg2}, K_{pg4}, K_{ig2}, and K_{ig4} are the proportional and integral gain coefficients of the PI controller in the GSC inner control loop, respectively.

3.2.2 Power system small signal analysis

In this study, we intend to design WADC for WTS. Therefore, additional control signals u_p, and u_q, as illustrated in Fig. 3.1, are regarded as inputs, while power flow in each transmission line is considered as system output.The power flow through lines measured by Phasor Measure Ment Units (PMUs) are fed as wide-area feedback signal to H_∞ controller that generates control signals u_p and u_q as shown in Fig. 3.1. The entire system, with WTS, is then linearized between inputs and outputs once stable equilibrium points are identified through load flow analysis. The system's state-space small signal model is represented as follows:

$$\begin{cases} p\Delta x = A\Delta x + B_i \Delta u_i \\ \Delta y_i = C_i \Delta x + D_i \Delta u_i \end{cases} \tag{3.8}$$

where Δ represent a small deviation, $x \in \Re^{(m\times 1)}$, $u \in \Re^{(n\times 1)}$, and $y \in \Re^{(o\times 1)}$ represent the system state, input, and output vectors, respectively; $A \in \Re^{(m\times m)}$, $C \in \Re^{(o\times m)}$, $B \in$

$\Re^{(m\times n)}$, and $D \in \Re^{(o\times n)}$ represent the system output, input, and feed-forward matrices, respectively; and m, n, and o represent the number of the system state, input, and output variables, respectively.

3.2.2.1 Time delay in feedback signal

The remote/wide-area signals are measured by PMUs in the power system and then sent over communication channels to WADC. The performance of WADC is degraded by the communication delay associated with wide-area signals and the introduction of phase deviation into the system. As a result, when designing WADC, it is necessary to account for the time delays brought on by wide-area signals. Time delays are commonly described by a first-order Pad'e approximation [46] with the following transfer function:

$$G_{(T_d)}(s) = \frac{1 - 0.5T_d s}{1 + 0.5T_d s} \tag{3.9}$$

where T_d denotes the delay time. It can be expressed in state-space representation as follows:

$$\begin{cases} p\Delta x_{T_d} = A_{T_d}\Delta x_{T_d} + B_{T_d}\Delta u_{T_d} \\ \Delta y_{T_d} = C_{T_d}\Delta x_{T_d} + D_{T_d}\Delta u_{T_d} \end{cases} \tag{3.10}$$

where the time delay in system state, output vector, and input vector are denoted by x_{T_d}, y_{T_d}, and u_{T_d}, respectively. The delay-free system model described in (3.8) can be combined in cascade with (3.10) to make a system with a time delay model of the power system as follows:

$$\begin{cases} p\Delta x_d = A_d\Delta x_d + B_{id}\Delta u_{id} \\ \Delta y_{id} = C_{id}\Delta x_d + D_{id}\Delta u_{id} \end{cases} \tag{3.11}$$

where the state, input, and output matrices for the relevant time-delay power system are given as follows:

$$A_d = \begin{bmatrix} A & 0 \\ B_{Td}C & A_{Td} \end{bmatrix}, B_{id} = \begin{bmatrix} B_i \\ B_{Td}D \end{bmatrix}, C_{id} = \begin{bmatrix} D_{Td}C & C_{Td} \end{bmatrix} \tag{3.12}$$

3.2.2.2 Feedback loop selection

The relevant dominant inter-area oscillation modes are determined using modal analysis of the time-delay power system model (3.11). This research uses geometric measurements to pick the control loop (i.e., feedback signal) for the WADC since they can assess the

relative strength of a signal and a controller's performance compared to a specific mode. The Geometric Measure of Observability (GMO) $gm_{oj}(k)$ is calculated using (2.24) of chapter-2.

The chosen feedback loop of the WADC should have the larger GMO to the dominant inter-area oscillation mode.

3.2.3 The dynamic impacts of WTS integration on system LFO modes

The system configuration and load flow remain identical when the conventional SG is replaced by the same capacity of WTS. However, the dynamic interaction between WTS and the Rest of the Power System (RPS) may affect the low-frequency oscillations in power system and may deteriorate small signal stability [78]. Wide-Area Damping Controller designed by ignoring dynamic interaction between WTS and RPS may not be effective in determining critical modes of oscillations in WTS integrated system. Therefore, in order to study impact of dynamic interaction between WTS and RPS, this work has investigated low-frequency oscillations in the system with and without WTS.

The change in power exchange $P_{WTS}+jQ_{WTS}$ between the WTS and the RPS (shown in Fig. 3.1) is the primary cause of the dynamic interaction. This analysis investigates a multi-machine power system in which WTS has replaced an SG and is separated into two open-loop subsystems: the WTS that has replaced a SG, and the RPS. The subsystem of the WTS has already been discussed in Section 3.2. The RPS subsystem includes all the remaining SGs, loads, and transmission systems. The linearized state equations of the RPS and the synchronous generator G that is being replaced by WTS, at the steady-state operating condition are as follows:

$$\begin{cases} p\Delta x_{RPS} = A_{RPS}\Delta x_{RPS} + B_{RPS}\Delta u_{RPS} \\ \Delta y_{RPS} = C_{RPS}\Delta x_{RPS} + D_{RPS}\Delta u_{RPS} \end{cases} \tag{3.13}$$

$$\begin{cases} p\Delta x_G = A_G\Delta x_G + B_G\Delta u_G \\ \Delta y_G = C_G\Delta x_G + D_G\Delta u_G \end{cases} \tag{3.14}$$

$$\begin{cases} \Delta u_{RPS} = [\Delta P_{RPS} \;\; \Delta Q_{RPS}]^T, \Delta y_{RPS} = [\Delta V_{RPS} \; \Delta\theta_{RPS}]^T \\ \Delta y_G = [\Delta V_G \;\; \Delta\theta_G]^T, \Delta u_G = [\Delta P_G \;\; \Delta Q_G]^T \end{cases} \tag{3.15}$$

where Δx_{RPS} represents the state vector of the RPS excluding the SG that is being replaced by the WTS, and Δx_G is the state vector of the replaced SG. y and x are output and state variable vectors, respectively. u_{RPS}, and u_G are the input of the RPS and replaced SG, respectively, and T specifies the transposition.

When a SG is replaced by the WTS, the linearized state model of the WTS at the steady-state operating condition is as follows:

$$\begin{cases} p\Delta x_{WTS} = A_{WTS}\Delta x_{WTS} + B_{WTS}\Delta u_{WTS} \\ \Delta y_{WTS} = C_{WTS}\Delta x_{WTS} + D_{WTS}\Delta u_{WTS} \end{cases} \tag{3.16}$$

where $\Delta y_{WTS} = [\Delta V_{WTS} \quad \Delta\theta_{WTS}]^T$ represents the WTS input, $\Delta u_{WTS} = [\Delta P_{WTS} \quad \Delta Q_{WTS}]^T$ represents the WTS output, and Δx_{WTS} represents state vector for WTS.

The following steps are applied to examine the impact of system dynamics in LFO mode for WTS replacing SG:

1). Execute modal analysis of the system (3.8) and determine the LFO modes $\lambda_i, i = 1, 2, ...$

2). Derive the state model of the power system with replaced SG and remaining SGs in the system from (3.13) and (3.14), determine the power system LFO modes from the state matrix $A_{(RPS)+G)}$ as $\lambda_{Gi}, i = 1, 2....$

3). Derive the state model of the power system with SG replaced by the WTS from (3.13) and (3.16) and determine the power system LFO modes from the state matrix $A_{(RPS)+WTS}$ as $\lambda_{WTSi}, i = 1, 2...$

The impact of the dynamic interaction between replaced SG and RPS and the dynamic interaction between the WTS and RPS can be calculated using (3.17).

$$\begin{cases} \Delta\lambda_{Gi} = \lambda_{Gi} - \lambda_i \\ \Delta\lambda_{WTSi} = \lambda_{WTSi} - \lambda_{Gi} \end{cases} \tag{3.17}$$

The entire impact on system LFO modes on replacing SG with WTS is determined as follows:

$$\Delta\lambda_i = \Delta\lambda_{Gi} + \Delta\lambda_{WTSi} = \lambda_{WTSi} - \lambda_i, i = 1, 2 \ldots \tag{3.18}$$

3.3 Design of Dual-Channel WADC for WTS

The supplementary damping controller connected to the WTS's reactive control loop mainly affects the reactive power output, whereas linked to the active control loop primarily influences the active power output. Also, the reactive and active power modulation utilized for damping control has distinct effects on the WTS dynamics. Therefore, a double-channel H_∞ control-based WADC is proposed in this work to control the reactive and active power of the WTS, simultaneously. This will give the WTS more flexibility to participate in the damping control and improve WTS dynamics.

3.3.1 Double-channel control structure and synthesis of H_∞ controller

Fig. 3.2 shows the double-channel WADC scheme for WTS. The damping controller for the outer control loop of RSC is designed based on the H_∞ control approach, where T stand for the transfer function for generalized plant, K for the transfer function of the controller, w for external inputs (taken as P_{sref} and Q_{sref} in this work), z for the regulated variables (taken as $(P_{sref} - P_s)$ and $(Q_{sref} - Q_s)$ in this work) which are being regulated by the controller), v for output measurements (taken as real power flow, P_L through lines being measured by PMUs), and control signals generated by H_∞ controller are represented by u. This work considers generation of control signal u_p for real power control and u_q for reactive power control. The H_∞ controller takes line flows measured by PMUs as input and generates control signals u_p and u_q to regulate error signals $(P_{sref} - P_s)$ and $(Q_{sref} - Q_s)$, respectively, for real and reactive power outer control loop of RSC, respectively, as shown in Fig. 3.1. The linear fraction transformation is used to obtain the closed-loop transfer function from w to z, denoted M_{zw}, as follows:

$$M_{zw} = Fl(T, K) = T_{zw} + T_{zu}K(I - T_{vu}K)^{-1}T_{vw} \tag{3.19}$$

To minimize the maximum gain of the control system closed-loop transfer function from w to z (i.e., $M_{zw}(\mathrm{s})$), the H_∞ optimum controller must identify a stabilizing function K. An H_∞ norm can characterize this gain as,

$$\|M_{zw}\|_\infty = \overset{\max}{\omega}\bar{\sigma}(M_{zw}(j\omega)) = \gamma_{\min} < \gamma \tag{3.20}$$

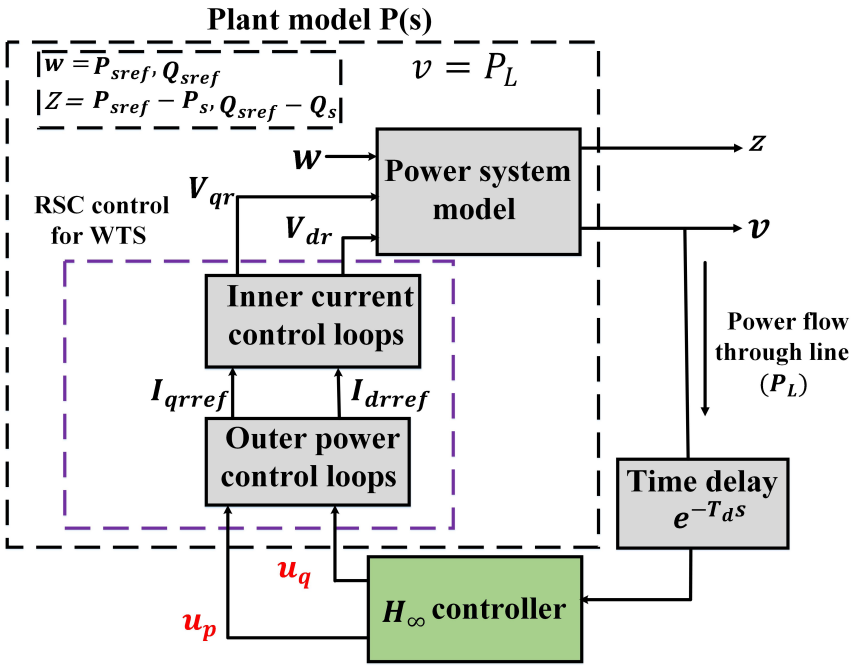

Figure 3.2: The design scheme for double-channel H_∞ controller.

The conventional two-Riccati equation [79] can be used to find the optimum solution of (3.20), which is denoted as $\gamma_{\min}$ and solved using MATLAB-based *hinfsyn* function. The H_∞ suboptimal problem is defined as a suitable value $\gamma < \gamma_{\min}$ to approach the optimal value $\gamma_{\min}$ using the γ -iteration technique. A nominal system γ may have been set to 1.

3.3.2 Procedure to design proposed WADC

The following steps are provided for designing a double-channel H_∞ WADC for WTS:

1. Linearize the system with the integration of WTS about a stable equilibrium point.

2. Find the system's inter-area oscillation modes using modal analysis and identify the prominent inter-area oscillation modes based on frequency and damping ratio.

3. Using the geometric measure observability method, identify the appropriate time-delayed feedback signals for the prominent inter-area oscillation modes.

4. Reduce the linearized system with P_s, and Q_s, as input and the appropriate feedback signal as the output using the Schur model reduction technique [44] so that it contains the prominent inter-area oscillation modes.

5. Obtain augmented plant model from the reduced order system model using (3.19) and solve H_∞ control problem using *hinfsyn* function in MATLAB.

6. For the augmented plant model, design the optimal H_∞ controller by minimizing the H_∞ norm using (3.20).

3.4 Validation on New England Ten-Machine System

3.4.1 Description of study system and eigenvalue analysis

The case studies were performed on modified New England ten-machine system to study the inter-area oscillations damping performance of the proposed double-channel H_∞ control-based WADC in WTS integrated power network. The details of the system are given in Appendix-C. This practical study system is divided into three areas, as depicted in Fig. 3.3. The SG1-SG3 are in Area 1, SG8-SG10 are in Area 2, and SG4-SG7 are in Area 3. A comprehensive description of this test system is found in [80]. Each Synchronous Generator (SG) is described by a 6th-order model equipped with an IEEE type I excitation system and a governor type I, except SG1, which represents the external equivalent generator. Furthermore, all loads in the study system are modelled as constant impedances.

This practical test system without Power System Stabilizer (PSS) and with PSS is referred to in this work as case-1 (CS1) and case-2 (CS2), respectively. The eigenvalues and damping ratios (ξ) of the test system under steady-state operating condition are shown in Table 3.1. This test system has four inter-area modes in CS1, namely M1, M2, M3, and M4 modes. It is clear that the prominent inter-area modes, M1 and M4, have damping ratios below 5% for CS1 case, as shown in Table 3.1.

To stabilize the system's dominating inter-area modes in CS1, PSSs are placed on the dominant SGs in three areas (i.e., SG2, SG4, and SG10). The PSS parameters are taken from [81], and a genetic algorithm tunes the parameters of PSS. Table 3.1 shows the system inter-area oscillation modes in CS1 and CS2 under normal operating conditions. The damping ratios of dominant inter-area modes M1 and M4 are obtained as 4.74% and 3.24% in CS1, which get increased to 11.6% and 10.11%, respectively, in CS2. Furthermore, other modes' damping performance are also enhanced in CS2 compared to CS1.

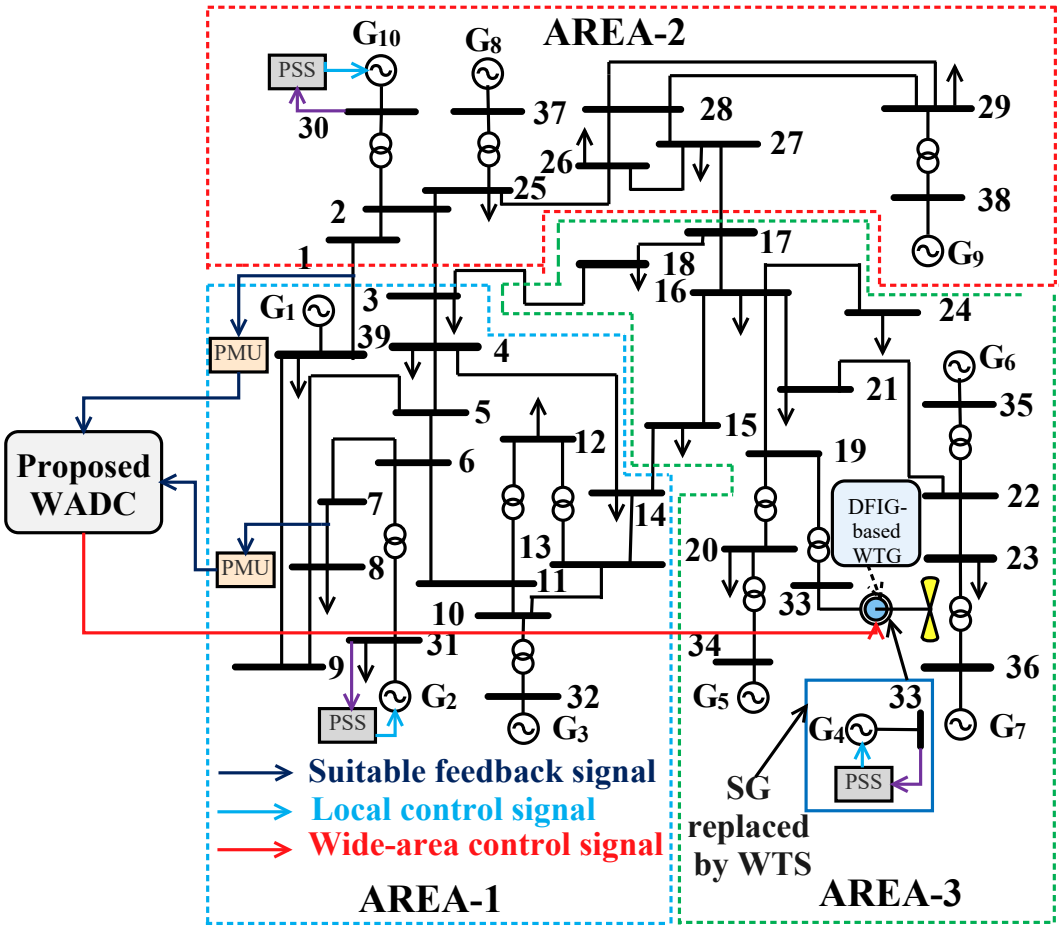

Figure 3.3: A modified New England ten-machine system for case CS4 with WTS replacing SG4.

3.4.2 WTS integration scenario

To observe the impact of system damping in the inter-area modes under the change in system inertia, the DFIG-based WTS is integrated into the system. The total inertia constant of the New-England ten-machine system in the absence of WTS is obtained by summing the inertia constant of all conventional SGs on a 100 MVA base. Thereafter, one conventional SG is replaced with the aggregate model of a DFIG-based WTS of the same capacity. Considered case-3 (CS3) is the dominant synchronous generator SG2 with PSS in Area-1 replaced by WTS of the same capacity to decrease the system inertia from 782.2s to 752.2s. The dominant synchronous generator SG4 with PSS in Area-3 replaced by WTS of the same capacity to decrease the system inertia from 782.2s to 754s is referred to as case-4 (CS4). The dominant synchronous generator SG10 with PSS in Area-2 replaced by WTS of the same capacity to lower the system inertia from 782.2s to 740s is referred to as case-5 (CS5). Fig. 3.3 is drawn for case CS4.

Table 3.1: Eigenvalues and Damping ratio of the study system under CS1 and CS2

Inter-area mode	**Eigenvalue and damping ratio in CS1**	**Modes shape in CS1**	**Eigenvalue and damping ratio in CS2**
M1	$\mathbf{-0.276 \pm i5.817}$ ($\boldsymbol{\xi = 4.74\%}$, $\boldsymbol{f = 0.925Hz}$)	$\boldsymbol{G_2}$ **vs** $\boldsymbol{G_4}$ **(Area-1 vs Area-3)**	$\mathbf{-0.450 \pm i3.854}$ ($\boldsymbol{\xi = 11.6\%}$, $\boldsymbol{f = 0.613Hz}$)
M2	$-0.3456 \pm i5.446$ ($\xi = 6.33\%$, $f = 0.866Hz$)	G_9, G_{10} vs G_2, G_3, G_4 (Area-2 vs Area (1 & 3))	$-0.417 \pm i3.970$ ($\xi = 10.46\%$, $f = 0.631Hz$)
M3	$-0.302 \pm i4.986$ ($\xi = 6.05\%$, $f = 0.793Hz$)	G_2, G_3, G_4 vs G_{10} (Area (1 & 3) vs Area-2)	$-0.490 \pm i3.879$ ($\xi = 12.55\%$, $f = 0.617Hz$)
M4	$\mathbf{-0.121 \pm i3.731}$ ($\boldsymbol{\xi = 3.24\%}$, $\boldsymbol{f = 0.593Hz}$)	$\boldsymbol{G_2, G_3,}$ **vs** $\boldsymbol{G_4, G_8, G_{10}}$ **(Area-1 vs Area (2 & 3)**	$\mathbf{-0.400 \pm i3.942}$ ($\boldsymbol{\xi = 10.11\%}$, $\boldsymbol{f = 0.627Hz}$)

The WTS of each case from CS3 to CS5 operates in three scenarios: S1 (with a wind speed of 7 m/s, the rotor speed of the WTS 0.75 p.u., regarded as sub-synchronous operating condition), S2 (with a wind speed of 9 m/s, the rotor speed of the WTS 0.95 p.u., regarded as normal operating condition), and S3 (with a wind speed of 11 m/s, the rotor speed of the WTS 1.15 p.u., regarded as super-synchronous operating condition).

Table 3.2 illustrates the effect of WTS integration on the study system in damping of inter-area oscillation modes in cases CS3, CS4, and CS5 under scenario S1. The damping ratio of dominant inter-area mode M4 under S1 gets decreased to 6.02% in CS3, 6.61% in CS4 and 6.18% in CS5 compared to the value of 10.11% when combination of SG and PSS was not replaced by WTS (Table 3.1). Similar observations are made for dominant mode M1. This shows that replacement of SG with PSS by WTS of same MVA capacity deteriorated damping of dominant inter-area modes.

The damping ratio of the concerned inter-area modes of the system in CS3, CS4, and CS5 under scenario S2 are illustrated in Table 3.3. In CS3 under scenario S2, the damping ratios of modes M1 and M4 are calculated to be 7.22% and 6.09%, respectively. In CS4, these ratios are 7.51% and 6.62%, respectively, while these are, 6.67% and 6.31%,respectively, in CS5. It is observed from Table 3.1 and Table 3.3 that replacement of SG plus PSS with WTS deteriorates damping under normal operating condition, too.

Table 3.2: Damping performance of the inter-area modes under scenario S1 operation of WTS

Inter-area mode	**Integration of WTS in CS3**	**Integration of WTS in CS4**	**Integration of WTS in CS5**
M1	$\mathbf{-0.357 \pm i5.036}$ $(\boldsymbol{\xi = 7.07\%})$	$\mathbf{-0.316 \pm i4.505}$ $(\boldsymbol{\xi = 7.00\%}\ )$	$\mathbf{-0.301 \pm i4.636}$ $(\boldsymbol{\xi = 6.48\%}\ )$
M2	$-0.415 \pm i5.265$ $(\xi = 7.86\%)$	$-0.399 \pm i5.227$ $(\xi = 7.62\%)$	$-0.395 \pm i5.705$ $(\xi = 6.92\%)$
M3	$-0.332 \pm i4.586$ $(\xi = 7.22\%)$	$-0.399 \pm i5.413$ $(\xi = 7.35\%)$	$-0.377 \pm i5.23$ $(\xi = 7.18\%)$
M4	$\mathbf{-0.166 \pm i2.764}$ $(\boldsymbol{\xi = 6.02\%})$	$\mathbf{-0.341 \pm i5.146}$ $(\boldsymbol{\xi = 6.61\%})$	$\mathbf{-0.270 \pm i4.371}$ $(\boldsymbol{\xi = 6.18\%})$
M5	$\mathbf{0.0504 \pm i1.256}$ $(\boldsymbol{\xi = -4\%})$	$---$	$\mathbf{0.0534 \pm i0.836}$ $(\boldsymbol{\xi = -6.387\%})$
$---$ Not observed			

Table 3.3: Damping performance of the inter-area modes under scenario S2 operation of WTS

Inter-area mode	**Integration of WTS in CS3**	**Integration of WTS in CS4**	**Integration of WTS in CS5**
M1	$\mathbf{-0.320 \pm i4.423}$ $(\boldsymbol{\xi = 7.22\%})$	$\mathbf{-0.335 \pm i4.45}$ $(\boldsymbol{\xi = 7.51\%})$	$\mathbf{-0.307 \pm i4.59}$ $(\boldsymbol{\xi = 6.67\%})$
M2	$-0.407 \pm i4.650$ $(\xi = 8.72\%)$	$-0.387 \pm i5.035$ $(\xi = 7.67\%)$	$-0.379 \pm i5.269$ $(\xi = 7.17\%)$
M3	$-0.404 \pm i5.252$ $(\xi = 7.67\%)$	$-0.402 \pm i5.445$ $(\xi = 7.37\%)$	$-0.384 \pm i5.703$ $(\xi = 6.73\%)$
M4	$\mathbf{-0.320 \pm i4.957}$ $(\boldsymbol{\xi = 6.09\%})$	$\mathbf{-0.349 \pm i5.262}$ $(\boldsymbol{\xi = 6.62\%}\ )$	$\mathbf{-0.349 \pm i5.522}$ $(\boldsymbol{\xi = 6.31\%})$

In cases, CS3, CS4, and CS5 under operating scenario S3, Table 3.4 shows the damping performance of the relevant inter-area modes. The modal analysis results shown in Table 3.4 demonstrates that when the WTS operates in scenario S3, the inter-area modes' system damping capabilities are lower than in scenarios S1 and S2. Scenario S3 results shown in Table 3.4 also demonstrate damping deterioration when SG-PSS combination is replaced by WTS of same rating.

It is observed from Table 3.2 and Tables 3.4 that replacement of SG2 with PSS by WTS (case CS3) leads to a new critical mode M5 that has negative damping with

Table 3.4: Damping performance of the inter-area modes under scenario S3 operation of WTS

Inter-area mode	**Integration of WTS in CS3**	**Integration of WTS in CS4**	**Integration of WTS in CS5**
M1	$\mathbf{-0.215 \pm i3.878}$ $(\boldsymbol{\xi = 5.54\%}$)	$\mathbf{-0.351 \pm i5.05}$ $(\boldsymbol{\xi = 6.94\%})$	$\mathbf{-0.300 \pm i4.758}$ $(\boldsymbol{\xi = 6.629\%})$
M2	$-0.387 \pm i5.321$ $(\xi = 7.26\%)$	$-0.408 \pm i5.424$ $(\xi = 7.50\%)$	$-0.381 \pm i5.677$ $(\xi = 6.71\%)$
M3	$-0.316 \pm i4.356$ $(\xi = 7.25\%)$	$-0.324 \pm i4.414$ $(\xi = 7.32\%)$	$-0.287 \pm i3.822$ $(\xi = 7.51\%)$
M4	$\mathbf{-0.241 \pm i5.092}$ $(\boldsymbol{\xi = 4.73\%})$	$\mathbf{-0.346 \pm i5.521}$ $(\boldsymbol{\xi = 6.57\%})$	$\mathbf{-0.299 \pm i5.5452}$ $(\boldsymbol{\xi = 5.48\%})$
M5	$\mathbf{0.0163 \pm i0.892}$ $(\boldsymbol{\xi = -1.827\%})$	$\mathbf{---}$	$\mathbf{0.0243 \pm i0.984}$ $(\boldsymbol{\xi = -2.468\%})$
$---$ Not observed			

eigenvalues in right half of complex plane for sub-synchronous operation (scenario S1) as well as super-synchronous operation (scenario S3). On the same line, replacement of SG10 with PSS by WTS (case CS5) also introduces a new critical mode M5 that has negative damping with eigenvalues located in right half of complex plane for sub-synchronous operation (scenario S1) as well as super-synchronous operation (scenario S3). This indicates that dynamic interaction between WTS and RPS makes the system unstable for cases CS3 and CS5 under scenarios S1 and S3. Though system remains stable under normal operating conditions (scenario S2, Table 3.3) for all the three cases (viz cases CS3, CS4 and CS5), damping deteriorates if combination of SG and PSS is replaced by WTS of same capacity. Therefore, design of WADC for the system must include dynamic interaction of WTS with RPS else controller will not be very effective in damping inter-area oscillations and improving small signal stability.

Participation of each SG in dominant oscillation mode M4 as a result of WTS integration under scenario S1 in low system inertia condition is illustrated in Fig. 3.4. Under scenario S1, it is observed that SG4 is the most dominant generator in cases CS3 and CS5, whereas SG10 is the dominant generator in CS4.

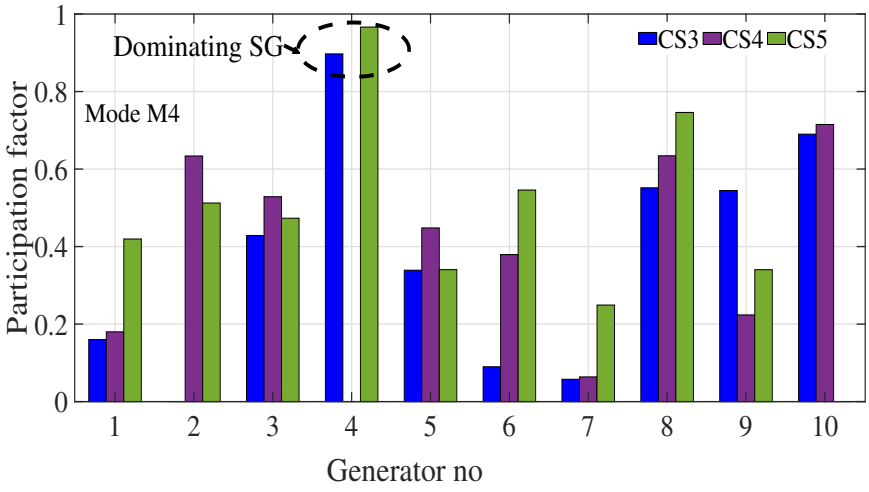

Figure 3.4: SG participation in the inter-area mode M4 with the integration of WTS operating under scenario S1.

3.4.3 The dynamic impact of control mode in the inter-area mode under the change in system inertia condition

The relative contribution of each state variable is assessed using participation factor analysis [82], which is used to investigate the main contributors of the dominant inter-area oscillation mode. Fig. 3.5 shows the contribution of state variables in the dominating inter-area oscillation mode M1 of the study test system with the integration of WTS in cases CS4 and CS5 under scenario S1.

As can be seen from Fig. 3.5, the main contributors to the dominant inter-area oscillation mode M1 of the system with integration of WTS in cases CS4 and CS5 under the scenario S1 are: ω, and δ of SGs; ω_t, ω_r, and T_g for drive train of WTS; $\psi_{qs}, \psi_{ds}, \psi_{qr}$, and ψ_{dr} corresponding to flux linkages of induction generator; $x_{qr1}, x_{qr2}, x_{dr1}$ and x_{dr2} for RSC of WTS; $x_{qg1}, x_{qg2}, x_{dg1}$, and x_{dg2} for GSC of WTS. As state variables of the SG as well as of the WTS contribute to the dominant inter-area oscillation mode, it can be understood that there is close control loop interaction between SGs and WTS. Furthermore, when WTS is integrated into CS5, the contributions of $x_{qr1}, x_{qr2}, x_{dr1}$, x_{dr2}, x_{dg1}, and x_{dg2} are significantly higher than when WTS is integrated into CS4, indicating that the impact of WTS control system on the inter-area oscillation will increase under the condition of low system inertia as case CS5 has lower inertia (740s) compared to case CS4 (754s). So, in addition to the system's low inertia, another factor affecting the inter-area oscillation of the power system with the integration of WTS is the close control loop

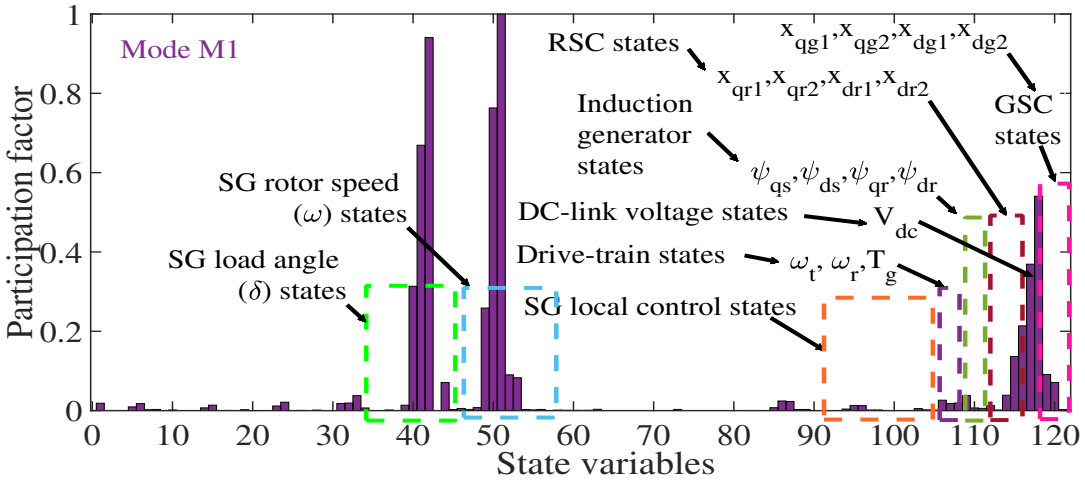

(a)

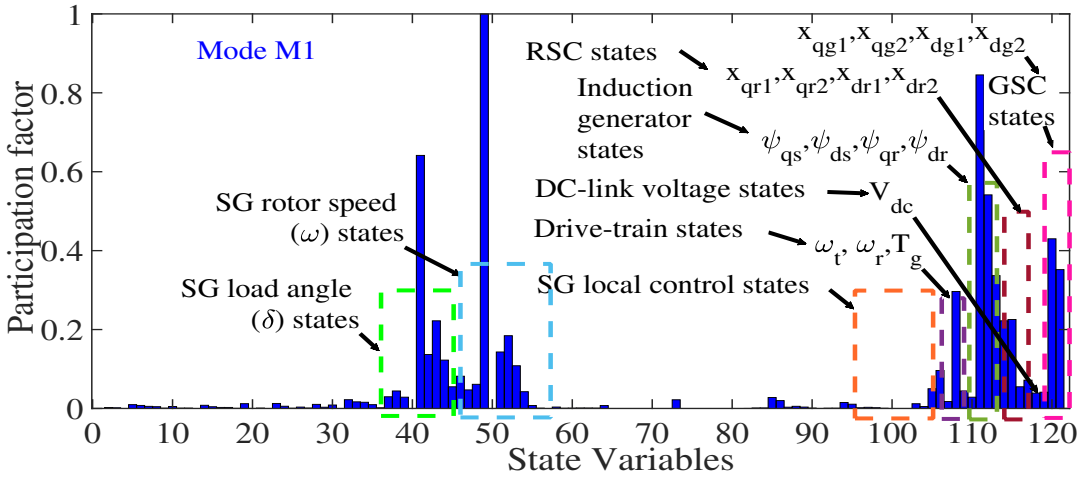

(b)

Figure 3.5: Participation factors of the modified New England ten-machine system in critical inter-area mode. (a) Integration of WTS in CS4 under scenario S1 (b) Integration of WTS in CS5 under scenario S1.

interaction between SGs and WTS under low system inertia conditions.

3.4.4 Designing WADC for WTS

The position of the damping controller and the suitable feedback signal are selected as the initial steps in designing the proposed WADC for WTS. Using the GMO methods described in Section 3.2.2.1, the damping controller feedback signal is selected. We have also taken into account the feedback signal's 100 ms and 200 ms communication time delays in this work. The GMO of the practical system of all transmission line's active

powers for dominant inter-area modes M1 and M4 are illustrated in Fig. 3.6. As can be observed, line 1-39 has maximum observability for mode M1, whereas, line 7-8 has maximum observability for mode M4. Therefore, the active power flow in these lines are chosen as the feedback signals for the WADC, and these signals are measured by PMUs installed at test system buses 39 and 8, respectively. WTS active and reactive power are selected as the control variables to design WADC as these have major impact in controlling dominant inter-area oscillation modes.

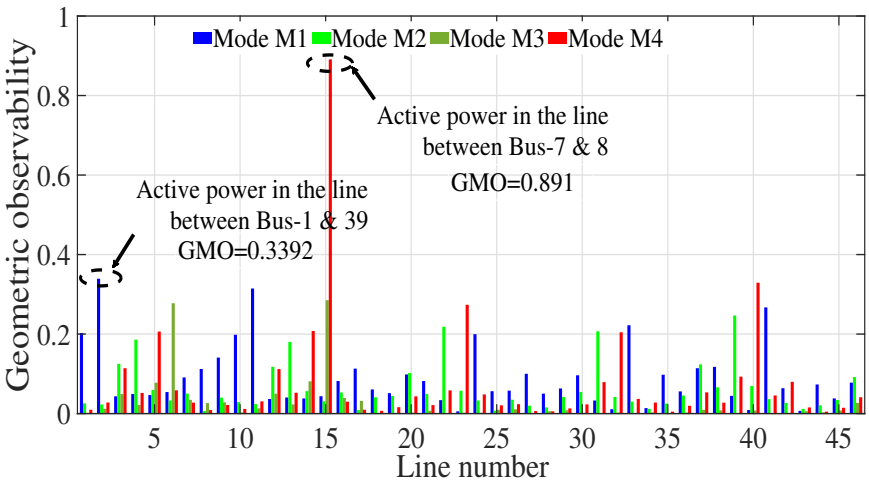

Figure 3.6: Geometric observability measure for line active power.

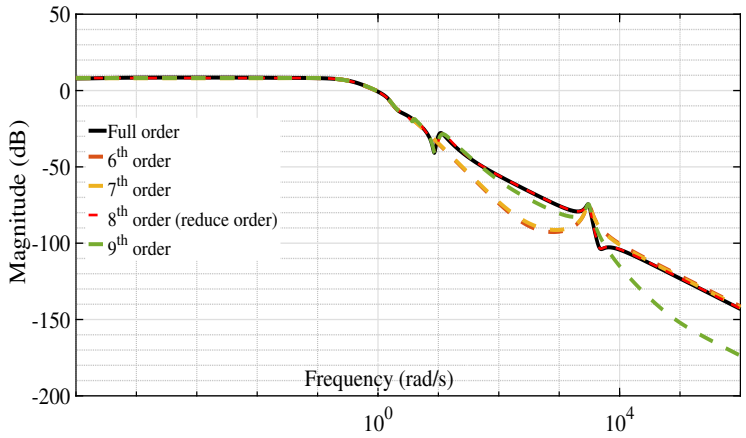

Figure 3.7: Frequency responses of full-order and reduced-order models of the modified New England ten-machine system.

The plant model's outputs, P_{7-8}, and P_{1-39}, and the P_s, and Q_s, inputs for the integration of WTS in CS4 under scenario S2 with a 100 ms continuous time delay in feedback signals are used to determine the system's order, which is found to be 121. The

complexity of the WADC design is decreased by reducing this higher-order system to an 8th-order system using the Schur model reduction method [44]. The frequency response of the 8th-order reduced system is approximately the same as that of the full-order system in the frequency range of (0.1-2) Hz, as depicted in Fig. 3.7. The reduced order system contains the significant inter-area oscillation modes M1 and M4. The MATLAB function *schurmr* is utilized for reducing the full-order system model to a reduced-order power system model. The transfer function of the reduced order system is as follows:

$$G_{red}(s) = \frac{N_{red}(s)}{D_{red}(s)} \tag{3.21}$$

where $N_{red}(s) = -1.261s^7 - 2422s^6 - 5.926 \times 10^4 s^5 + 60656 \times 10^7 s^4 - 5.236 \times 10^7 s^3 - 4.521 \times 10^8 s^2 - 1.95 \times 10^8 s - 3.813 \times 10^8$

$D_{red}(s) = s^8 - 1660s^7 + 9.381 \times 10^5 s^6 - 5.177 \times 10^7 s^5 - 2.178 \times 10^8 s^4 - 4.784 \times 10^8 s^3 - 9.213 \times 10^8 s^2 - 5.198 \times 10^8 s - 2.555 \times 10^8$

3.4.4.1 Design of double-channel H_∞ WADC

It follows the proposed WADC design procedure provided in Section 3.3.2. The *hinfsyn* function in MATLAB is used to solve the H_∞ optimal control problem. The H_∞ norms for active power control loop (γ_P), and reactive power control loop (γ_Q), are 0.645 and 0.465, respectively, which means that the H_∞ norm is satisfied.

The transfer function of the H_∞ WADC scheme for the active power control loop of the RSC is derived from (3.19). The augmented plant model is constructed, taking into account P_{sref}, $P_{sref} - P_s$, and P_{7-8} as the external input, regulated variable, and measured output, respectively. This augmented plant model is utilized to design the controller based on the reduced-order power system model taken from (3.21). The designed H_∞ WADC transfer function of the active control loop for the RSC is as follows:

$$G_{HP}(s) = \frac{N_{HP}(s)}{D_{HP}(s)} \tag{3.22}$$

where $N_{HP}(s) = 3.903s^7 - 1.207s^6 + 7.08 \times 10^9 s^5 + 2.974 \times 10^10 s^4 + 6.529 \times 10^{10} s^3 + 1.256 \times 10^{11} s^2 + 7.086 \times 10^{10} s + 3.482 \times 10^{10}$

$D_{HP}(s) = s^8 + 2.472 \times 10^2 s^7 + 4.026 \times 10^5 s^6 + 1.009 \times 10^7 s^5 + 9.051 \times 10^9 s^4 + 7.13 \times 10^9 s^3 + 6.151 \times 10^{10} s^2 + 2.654 \times 10^1 0s + 5.189 \times 10^{10}$

Similarly, the H_∞ WADC transfer function for the reactive power control loop of the RSC is derived from (3.19), considering Q_{sref}, $Q_{sref} - Q_s$, and P_{1-39} as the external input, regulated variable, and measured output, respectively. The design process utilizes the reduced-order model of the power system specified in (3.21). The resulting H_∞ WADC transfer function for the reactive control loop of the RSC is:

$$G_{HQ}(s) = \frac{N_{HQ}(s)}{D_{HQ}(s)} \tag{3.23}$$

where $N_{HQ}(s) = 3.107s^7 - 9.626s^6 + 5.64 \times 10^9 s^5 + 2.37 \times 10^{10} s^4 + 5.205 \times 10^{10} s^3 + 1.001 \times 10^{11} s^2 + 5.648 \times 10^{10} s + 2.776 \times 10^{10}$

$D_{HQ}(s) = s^8 + 1.973 \times 10^2 s^7 + 3.209 \times 10^5 s^6 + 8.05 \times 10^6 s^5 + 7.215 \times 10^9 s^4 + 5.685 \times 10^9 s^3 + 4.903 \times 10^{10} s^2 + 2.11 \times 10^1 0s + 4.137 \times 10^{10}$

Remark: The performance of a double-channel H_∞ control scheme in mitigating power system inter-area oscillations through active and reactive power control on the rotor side converter is influenced by key design parameters, including controller gain, control bandwidth, time delay compensation, controller structure and order, communication infrastructure, and operating constraints. Properly tuning these parameters is essential for achieving effective control while ensuring system stability.

3.4.5 Efficacy assessment of the proposed WADC

The impact of the proposed WADC in damping of relevant inter-area modes (M1 to M5) under the integration of WTS for cases CS3, CS4, and CS5, under scenarios S1, S2, and S3, considering time delays, are shown in Tables 3.5, 3.6, and 3.7, respectively. It is observed from Table 3.2, Table 3.3, and Table 3.4 that integration of WTS results in damping ratio less than 10% for modes M1 to M4 in the absence of WADC. However, proposed double-channel H_∞ controller based WADC results in significantly high damping of these modes, as observed from Table 3.5, Table 3.6, and Table 3.7. Furthermore, we compared the damping performance of proposed double-channel H_∞ scheme-based WADC with an existing PSS-based WADC presented in [83]. The results are shown in Table 3.5, Table 3.6, and Table 3.7 for cases CS3, CS4 and CS5,respectively. From modal analysis results

Table 3.5: Damping performance of proposed WADC for system inter-area modes with integration of WTS in Case CS3

Mode	T_d**(ms)**	**Scenario S1**		**Scenario S2**		**Scenario S3**	
		PSS-based WADC [83]	**Double-channel H_∞ WADC**	**PSS-based WADC [83]**	**Double-channel H_∞ WADC**	**PSS-based WADC [83]**	**Double-channel H_∞ WADC**
M1	**100**	$\mathbf{-0.412 \pm i3.641}$ $(\boldsymbol{\xi = 11.24\%})$	$\mathbf{-0.486 \pm i3.527}$ $(\boldsymbol{\xi = 13.65\%})$	$\mathbf{-0.520 \pm i4.123}$ $(\boldsymbol{\xi = 12.51\%})$	$\mathbf{-0.571 \pm i3.768}$ $(\boldsymbol{\xi = 14.98\%})$	$\mathbf{-0.325 \pm i3.363}$ $(\boldsymbol{\xi = 9.62\%})$	$\mathbf{-0.512 \pm i3.752}$ $(\boldsymbol{\xi = 13.64\%})$
	200	$\mathbf{-0.376 \pm i3.742}$ $(\boldsymbol{\xi = 10.04\%})$	$\mathbf{-0.472 \pm i3.812}$ $(\boldsymbol{\xi = 12.28\%})$	$\mathbf{-0.499 \pm i4.243}$ $(\boldsymbol{\xi = 11.68\%})$	$\mathbf{-0.541 \pm i3.658}$ $(\boldsymbol{\xi = 14.63\%})$	$\mathbf{-0.315 \pm i3.334}$ $(\boldsymbol{\xi = 9.40\%})$	$\mathbf{-0.481 \pm i3.731}$ $(\boldsymbol{\xi = 12.89\%})$
M2	100	$-0.463 \pm i3.92$ $(\xi = 11.81\%)$	$-0.493 \pm i3.62$ $(\xi = 13.49\%)$	$-0.531 \pm i4.350$ $(\xi = 12.11\%)$	$-0.601 \pm i4.023$ $(\xi = 14.93\%)$	$-0.398 \pm i4.01$ $(\xi = 9.92\%)$	$-0.491 \pm i3.672$ $(\xi = 13.37\%)$
	200	$-0.437 \pm i4.131$ $(\xi = 10.57\%)$	$-0.473 \pm i3.72$ $(\xi = 12.61\%)$	$-0.489 \pm i4.250$ $(\xi = 11.43\%)$	$-0.593 \pm i4.016$ $(\xi = 14.60\%)$	$-0.378 \pm i3.912$ $(\xi = 9.61\%)$	$-0.425 \pm i3.472$ $(\xi = 12.15\%)$
M3	100	$-0.392 \pm i3.475$ $(\xi = 11.20\%)$	$-0.420 \pm i3.12$ $(\xi = 13.34\%)$	$-0.592 \pm i4.486$ $(\xi = 13.08\%)$	$-0.572 \pm i4.013$ $(\xi = 14.113\%)$	$-0.371 \pm i3.95$ $(\xi = 9.39\%)$	$-0.431 \pm i3.231$ $(\xi = 13.46\%)$
	200	$-0.372 \pm i3.586$ $(\xi = 10.31\%)$	$-0.412 \pm i3.23$ $(\xi = 12.65\%)$	$-0.583 \pm i4.89$ $(\xi = 11.83\%)$	$-0.587 \pm i4.186$ $(\xi = 14.02\%)$	$-0.363 \pm i4.03$ $(\xi = 8.97\%)$	$-0.415 \pm i3.423$ $(\xi = 12.03\%)$
M4	**100**	$\mathbf{-0.386 \pm i3.32}$ $\mathbf{(\xi = 11.62\%)}$	$\mathbf{-0.398 \pm i3.11}$ $\mathbf{(\xi = 12.69\%)}$	$\mathbf{-0.503 \pm i4.013}$ $\mathbf{(\xi = 12.43\%)}$	$\mathbf{-0.585 \pm i3.798}$ $\mathbf{(\xi = 15.22\%)}$	$\mathbf{-0.378 \pm i3.91}$ $(\boldsymbol{\xi = 9.62\%})$	$\mathbf{-0.436 \pm i3.12}$ $(\boldsymbol{\xi = 13.97\%})$
	200	$\mathbf{-0.366 \pm i3.62}$ $(\boldsymbol{\xi = 10.06\%})$	$\mathbf{-0.396 \pm i3.21}$ $(\boldsymbol{\xi = 12.24\%})$	$\mathbf{-0.495 \pm i4.167}$ $(\boldsymbol{\xi = 11.79\%})$	$\mathbf{-0.533 \pm i3.781}$ $(\boldsymbol{\xi = 13.96\%})$	$\mathbf{-0.398 \pm i4.14}$ $(\boldsymbol{\xi = 9.56\%})$	$\mathbf{-0.412 \pm i3.24}$ $(\boldsymbol{\xi = 12.71\%})$
M5	100	$-0.146 \pm i1.225$ $(\xi = 11.84\%)$	$-0.186 \pm i1.246$ $(\xi = 14.76\%)$	– – –	– – –	$-0.098 \pm i0.981$ $(\xi = 9.95\%)$	$-0.128 \pm i0.978$ $(\xi = 12.97\%)$
	200	$-0.136 \pm i1.265$ $(\xi = 10.69\%)$	$-0.165 \pm i1.356$ $(\xi = 12.07\%)$	– – –	– – –	$-0.088 \pm i0.871$ $(\xi = 10.08\%)$	$-0.112 \pm i0.912$ $(\xi = 12.18\%)$
– – – Not observed							

shown in Tables 3.5, 3.6, and 3.7, we can observe that the proposed WADC damping performance is superior to the PSS-based WADC [83] under low system inertia conditions for all the cases considered. When considering time delay uncertainties, the proposed WADC can maintain dominant inter-area modes with damping ratio greater than 10%, whereas the existing PSS-based WADC has less than 10% damping ratio for some of the cases.

It is observed from Table 3.5 and Table 3.7 that mode M5 has positive damping under proposed double-channel H_∞ based WADC, and eigenvalues have negative real part. Thus, mode M5, which had negative damping with eigenvalues lying in the right half of the complex plane (Table 3.2 and Table 3.4), becomes a stable mode under proposed WADC. A comparison of results, in Table 3.5, Table 3.6 and Table 3.7 with results in Table 3.2, Table 3.3 and Table 3.4 show that other eigenvalues also get shifted more towards left under proposed WADC compared to cases when WADC was not put in the system. Thus, proposed WADC not only stabilizes unstable mode M5 but also enhances

Table 3.6: Damping performance of proposed WADC for system inter-area modes with integration of WTS in Case CS4

Mode	T_d(ms)	Scenario S1		Scenario S2		Scenario S3	
		PSS-based WADC [83]	Double-channel H_∞ WADC	PSS-based WADC [83]	Double-channel H_∞ WADC	PSS-based WADC [83]	Double-channel H_∞ WADC
M1	**100**	$\mathbf{-0.411 \pm i3.489}$ $(\boldsymbol{\xi = 11.71\%})$	$\mathbf{-0.473 \pm i2.669}$ $(\boldsymbol{\xi = 17.46\%})$	$\mathbf{-0.409 \pm i2.769}$ $(\boldsymbol{\xi = 14.62\%})$	$\mathbf{-0.502 \pm i2.065}$ $(\boldsymbol{\xi = 23.65\%})$	$\mathbf{-0.371 \pm i3.352}$ $(\boldsymbol{\xi = 10.46\%})$	$\mathbf{-0.582 \pm i3.701}$ $(\boldsymbol{\xi = 15.54\%})$
	200	$\mathbf{-0.561 \pm i4.56}$ $(\boldsymbol{\xi = 12.21\%})$	$\mathbf{-0.679 \pm i4.032}$ $(\boldsymbol{\xi = 16.60\%})$	$\mathbf{-0.626 \pm i4.54}$ $(\boldsymbol{\xi = 13.66\%})$	$\mathbf{-0.462 \pm i2.021}$ $(\boldsymbol{\xi = 22.85\%})$	$\mathbf{-0.415 \pm i4.031}$ $(\boldsymbol{\xi = 10.24\%})$	$\mathbf{-0.610 \pm i4.12}$ $(\boldsymbol{\xi = 14.64\%})$
M2	100	$-0.413 \pm i3.480$ $(\xi = 11.80\%)$	$-0.677 \pm i3.637$ $(\xi = 18.30\%)$	$-0.488 \pm i3.481$ $(\xi = 13.88\%)$	$-0.609 \pm i2.474$ $(\xi = 23.90\%)$	$-0.373 \pm i3.469$ $(\xi = 10.71\%)$	$-0.524 \pm i3.230$ $(\xi = 15.59\%)$
	200	$-0.452 \pm i4.01$ $(\xi = 11.27\%)$	$-0.698 \pm i4.056$ $(\xi = 17.20\%)$	$-0.584 \pm i4.345$ $(\xi = 13.32\%)$	$-0.598 \pm i2.74$ $(\xi = 21.32\%)$	$-0.466 \pm i4.836$ $(\xi = 9.59\%)$	$-0.618 \pm i4.15$ $(\xi = 14.72\%)$
M3	100	$-0.399 \pm i3.466$ $(\xi = 11.44\%)$	$-0.643 \pm i3.876$ $(\xi = 16.38\%)$	$-0.427 \pm i3.520$ $(\xi = 12.04\%)$	$-0.726 \pm i3.042$ $(\xi = 23.23\%)$	$-0.420 \pm i4.039$ $(\xi = 10.36\%)$	$-0.743 \pm i4.673$ $(\xi = 14.36\%)$
	200	$-0.432 \pm i3.89$ $(\xi = 11.04\%)$	$-0.648 \pm i4.042$ $(\xi = 15.82\%)$	$-0.552 \pm i4.29$ $(\xi = 12.86\%)$	$-0.583 \pm i2.82$ $(\xi = 20.67\%)$	$-0.379 \pm i3.938$ $(\xi = 9.58\%)$	$-0.573 \pm i4.28$ $(\xi = 13.27\%)$
M4	**100**	$\mathbf{-0.401 \pm i3.548}$ $(\boldsymbol{\xi = 11.23\%})$	$\mathbf{-0.581 \pm i3.342}$ $(\boldsymbol{\xi = 17.14\%})$	$\mathbf{-0.443 \pm i3.502}$ $(\boldsymbol{\xi = 12.25\%})$	$\mathbf{-0.792 \pm i3.380}$ $(\boldsymbol{\xi = 22.82\%})$	$\mathbf{-0.384 \pm i3.619}$ $(\boldsymbol{\xi = 10.55\%})$	$\mathbf{-0.409 \pm i2.769}$ $(\boldsymbol{\xi = 14.62\%})$
	200	$\mathbf{-0.415 \pm i4.059}$ $(\boldsymbol{\xi = 10.17\%})$	$\mathbf{-0.638 \pm i3.69}$ $(\boldsymbol{\xi = 17.04\%})$	$\mathbf{-0.423 \pm i3.491}$ $(\boldsymbol{\xi = 12.02\%})$	$\mathbf{-0.421 \pm i2.003}$ $(\boldsymbol{\xi = 20.5\%})$	$\mathbf{-0.371 \pm i3.519}$ $(\boldsymbol{\xi = 10.48\%})$	$\mathbf{-0.569 \pm i4.15}$ $(\boldsymbol{\xi = 13.58\%})$
M5	100	– – –	– – –	– – –	– – –	– – –	– – –
	200	– – –	– – –	– – –	– – –	– – –	– – –
– – – Not observed							

stability margin. A comparison of results of proposed WADC with the existing PSS-based WADC [83] shows that proposed WADC in more effective in enhancing stability margin compared to existing controller (Table 3.5, Table 3.6, and Table 3.7). It is observed from tables 3.5, 3.6, and 3.7 that eigenvalues have more negative real part if proposed double-channel H_∞ WADC is used instead of the existing PSS-based WADC. Therefore, a higher stability margin is ensured if proposed double-channel H_∞ WADC is used instead of existing PSS-based WADC.

3.5 Real-Time Dynamic Simulation Validations

Using the graphical user interface of RSCAD FX 1.4, the dynamic simulation of the modified New England ten-machine system is performed on RTDS. The real-time digital simulation workflow is depicted in Fig 2.14 of chapter-2. Using time steps of 50 μs in the mainstep and 3.333 μs in the substep interface, the RTDS simulates the practical test system and WTS models. The IRIG-B signal is used to synchronize the GTSYNC card

Table 3.7: Damping performance of proposed WADC for system inter-area modes with integration of WTS in Case CS5

Mode	T_d(ms)	Scenario S1		Scenario S2		Scenario S3	
		PSS-based WADC [83]	Double-channel H_∞ WADC	PSS-based WADC [83]	Double-channel H_∞ WADC	PSS-based WADC [83]	Double-channel H_∞ WADC
M1	**100**	$\mathbf{-0.389 \pm i4.016}$ ($\boldsymbol{\xi = 9.64\%}$)	$\mathbf{-0.497 \pm i3.787}$ ($\boldsymbol{\xi = 13.01\%}$)	$\mathbf{-0.386 \pm i3.571}$ ($\boldsymbol{\xi = 10.74\%}$)	$\mathbf{-0.403 \pm i3.121}$ ($\boldsymbol{\xi = 12.80\%}$)	$\mathbf{-0.372 \pm i4.132}$ ($\boldsymbol{\xi = 8.96\%}$)	$\mathbf{-0.497 \pm i3.841}$ ($\boldsymbol{\xi = 12.83\%}$)
	200	$\mathbf{-0.369 \pm i3.891}$ ($\boldsymbol{\xi = 9.44\%}$)	$\mathbf{-0.437 \pm i3.687}$ ($\boldsymbol{\xi = 11.77\%}$)	$\mathbf{-0.382 \pm i3.687}$ ($\boldsymbol{\xi = 10.36\%}$)	$\mathbf{-0.398 \pm i3.231}$ ($\boldsymbol{\xi = 12.27\%}$)	$\mathbf{-0.367 \pm i4.112}$ ($\boldsymbol{\xi = 8.88\%}$)	$\mathbf{-0.489 \pm i3.976}$ ($\boldsymbol{\xi = 12.20\%}$)
M2	100	$-0.398 \pm i3.971$ ($\xi = 9.97\%$)	$-0.462 \pm i3.681$ ($\xi = 12.45\%$)	$-0.481 \pm i4.297$ ($\xi = 11.12\%$)	$-0.564 \pm i3.631$ ($\xi = 15.35\%$)	$-0.431 \pm i4.381$ ($\xi = 9.79\%$)	$-0.531 \pm i4.121$ ($\xi = 12.77\%$)
	200	$-0.378 \pm i4.01$ ($\xi = 9.38\%$)	$-0.457 \pm i3.887$ ($\xi = 11.67\%$)	$-0.432 \pm i4.191$ ($\xi = 10.25\%$)	$-0.543 \pm i3.871$ ($\xi = 13.89\%$)	$-0.391 \pm i4.131$ ($\xi = 9.42\%$)	$-0.528 \pm i4.341$ ($\xi = 12.07\%$)
M3	100	$-0.403 \pm i3.691$ ($\xi = 10.85\%$)	$-0.489 \pm i3.491$ ($\xi = 13.87\%$)	$-0.476 \pm i4.012$ ($\xi = 11.86\%$)	$-0.571 \pm i3.865$ ($\xi = 14.61\%$)	$-0.298 \pm i3.522$ ($\xi = 8.43\%$)	$-0.396 \pm i3.243$ ($\xi = 12.21\%$)
	200	$-0.421 \pm i4.326$ ($\xi = 9.68\%$)	$-0.461 \pm i3.596$ ($\xi = 12.71\%$)	$-0.456 \pm i4.181$ ($\xi = 10.84\%$)	$-0.526 \pm i3.995$ ($\xi = 13.05\%$)	$-0.301 \pm i3.622$ ($\xi = 8.28\%$)	$-0.387 \pm i3.422$ ($\xi = 11.23\%$)
M4	**100**	$\mathbf{-0.381 \pm i3.761}$ ($\boldsymbol{\xi = 10.07\%}$)	$\mathbf{-0.518 \pm i3.987}$ ($\boldsymbol{\xi = 12.88\%}$)	$\mathbf{-0.497 \pm i4.221}$ ($\boldsymbol{\xi = 11.69\%}$)	$\mathbf{-0.577 \pm i3.891}$ ($\boldsymbol{\xi = 14.66\%}$)	$\mathbf{-0.379 \pm i4.126}$ ($\boldsymbol{\xi = 9.14\%}$)	$\mathbf{-0.489 \pm i4.013}$ ($\boldsymbol{\xi = 12.09\%}$)
	200	$\mathbf{-0.372 \pm i3.971}$ ($\boldsymbol{\xi = 9.32\%}$)	$\mathbf{-0.471 \pm i3.867}$ ($\boldsymbol{\xi = 12.09\%}$)	$\mathbf{-0.458 \pm i4.381}$ ($\boldsymbol{\xi = 10.39\%}$)	$\mathbf{-0.537 \pm i3.912}$ ($\boldsymbol{\xi = 13.72\%}$)	$\mathbf{-0.381 \pm i4.226}$ ($\boldsymbol{\xi = 8.97\%}$)	$\mathbf{-0.469 \pm i4.131}$ ($\boldsymbol{\xi = 11.28\%}$)
M5	100	$-0.0861 \pm i0.832$ ($\xi = 10.29\%$)	$-0.0981 \pm i0.763$ ($\xi = 12.75\%$)	– – –	– – –	$-0.0796 \pm i0.871$ ($\xi = 9.10\%$)	$-0.0896 \pm i0.725$ ($\xi = 12.26\%$)
	200	$-0.0759 \pm i0.812$ ($\xi = 9.312\%$)	$-0.0898 \pm i0.788$ ($\xi = 11.39\%$)	– – –	– – –	$-0.0743 \pm i0.832$ ($\xi = 8.89\%$)	$-0.0856 \pm i0.801$ ($\xi = 10.62\%$)
– – – Not observed							

of the RTDS with a GPS clock. The WADC controller in the NovaCor with the mainstep receives measurement signals from the GTNET PMU of the simulator and switches the output to WTS.

The following contingencies are simulated in the study test system to assess the performance of the designed WADC for WTS integrated network.

- Contingency 1 (C1): A three-phase fault with a 0.1s duration is imposed at bus 20 in Area-3 at time t = 3s.

- Contingency 2 (C2): The three-phase fault is imposed on the transmission line between buses 28 and 29 at t = 3s for 0.1s, and the transmission line between buses 27 and 17 is permanently out of service.

The nonlinear simulation of each contingency case includes a 100 ms continuous time delay in the feedback signal of the WADC for WTS.

3.5.1 Contingency 1 (C1)

In the practical study system, the integration of WTS into CS4 (i.e., SG-4 with PSS replaced by WTS of the same capacity) is simulated under contingency C1. In this specific contingency scenario, the DFIG-based WTS operation was considered at three distinct induction generator speeds. These speeds are categorized as sub-synchronous, normal, and super-synchronous, referred to as scenarios S1, S2, and S3, respectively, in this study. These simulations are conducted to evaluate the damping performance of the proposed dual-channel H_∞ WADC for WTS.

The dynamic simulation response of the proposed WADC for WTS operated under scenario S1 is depicted in Fig 3.8. The dynamic response of power flow through line P_{1-39} and rotor speed deviation between SG2 and SG10 are shown in Fig 3.8 (a) and (b), respectively. It is seen that the power oscillation damping and SG rotor oscillation are effectively damped under the imposed fault. The dynamic response analysis reveals substantial reductions in peak overshoot and settling time compared to PSS-based WADC systems [83]. Additionally, Fig 3.8 (c) and (d) show the dynamic response of DFIG rotor speed and DC-link voltage between the grid and the rotor side converter, respectively. The dynamic simulation responses of d-axis grid side converter reference current and WTS active power are shown in Fig 3.8 (e) and (f), respectively. The dynamic simulation responses reveal that oscillations in the d-axis grid side converter reference current and WTS active power under contingency C1 are effectively diminished under operating scenario S1. Based on these simulation results, it becomes obvious that the proposed WADC exhibits superior damping performance in mitigating prominent inter-area oscillation modes compared to existing PSS-based WADC [83].

Additionally, when the WTS operates under scenario S2, the dynamic system response is depicted in Fig 3.9. Figures 3.9 (a) and (b) illustrate the dynamic behaviour of real power flow through line P_{1-39} and the rotor speed difference between SG2 and SG10, respectively. These simulation results reveal that power and rotor oscillations are effectively damped and exhibit superior damping performance compared to existing PSS-based WADC [83]. When the WTS operates in normal conditions, it maintains a balanced and effective inertia between the sub-synchronous and super-synchronous conditions. This equilibrium ineffective inertia is crucial as it empowers the DFIG to efficiently absorb and release energy during oscillations, thereby significantly enhancing its damping capa-

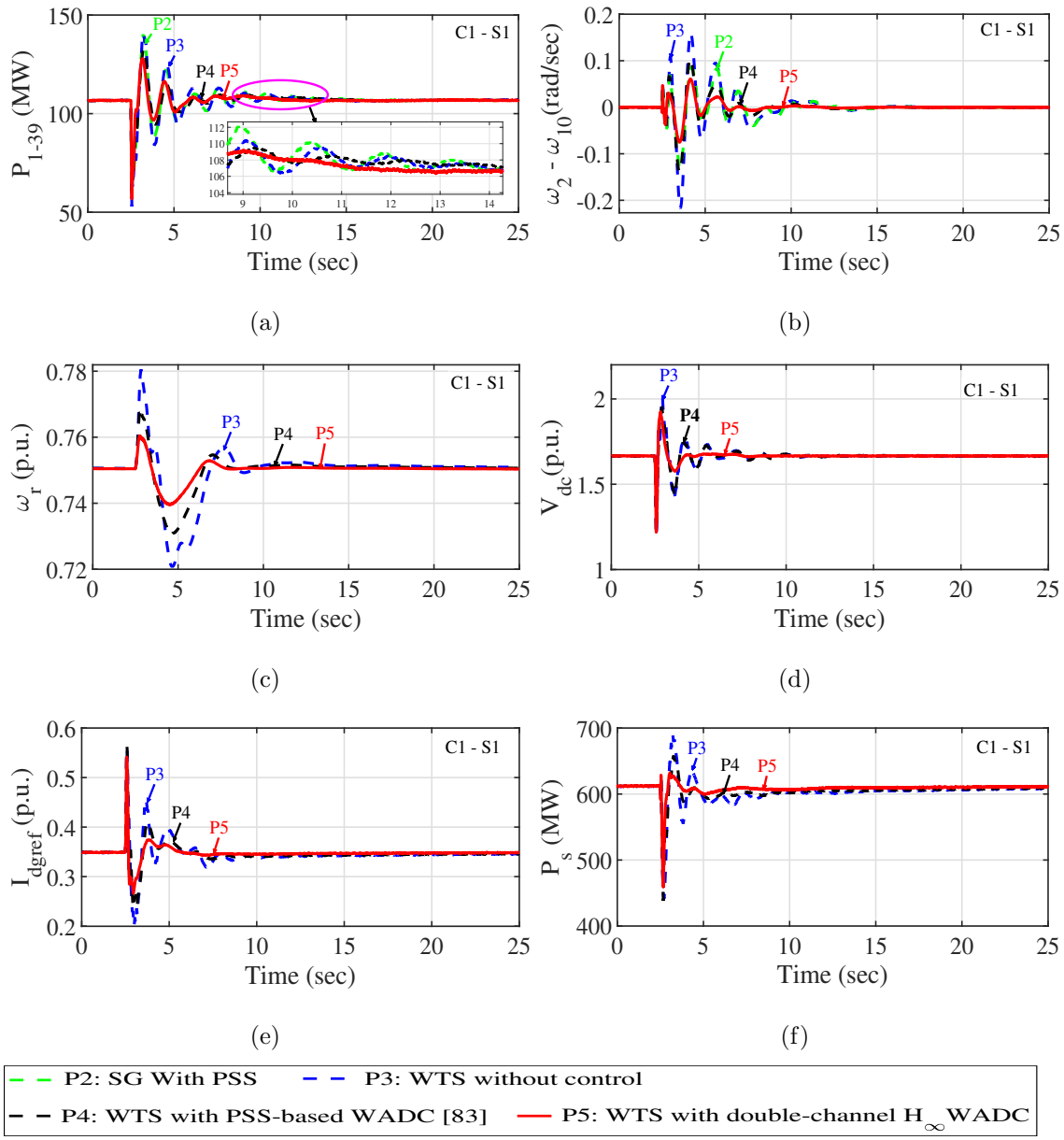

Figure 3.8: Dynamic response of the system with WTS integration in CS4 operating under scenario S1 for contingency C1. (a) Active power of line 1-39, (b) Rotor speed deviation between SG2 and SG10, (c) DFIG rotor speed, (d) DC-link voltage, (e) *d*-axis grid side converter reference current, and (f) WTS active power.

bility. Consequently, the proposed WADC for WTS, operating under normal conditions, offers superior damping capabilities for mitigating power system prominent inter-area oscillations compared to the sub-synchronous conditions of operation. Furthermore, it's worth noting that oscillations in DFIG rotor speed and DC-link voltage are also efficiently damped, as depicted in Fig 3.9 (c) and (d), respectively. In Fig. 3.9 (e), and (f), the dynamic simulation responses for the *d*-axis reference current of the grid-side converter

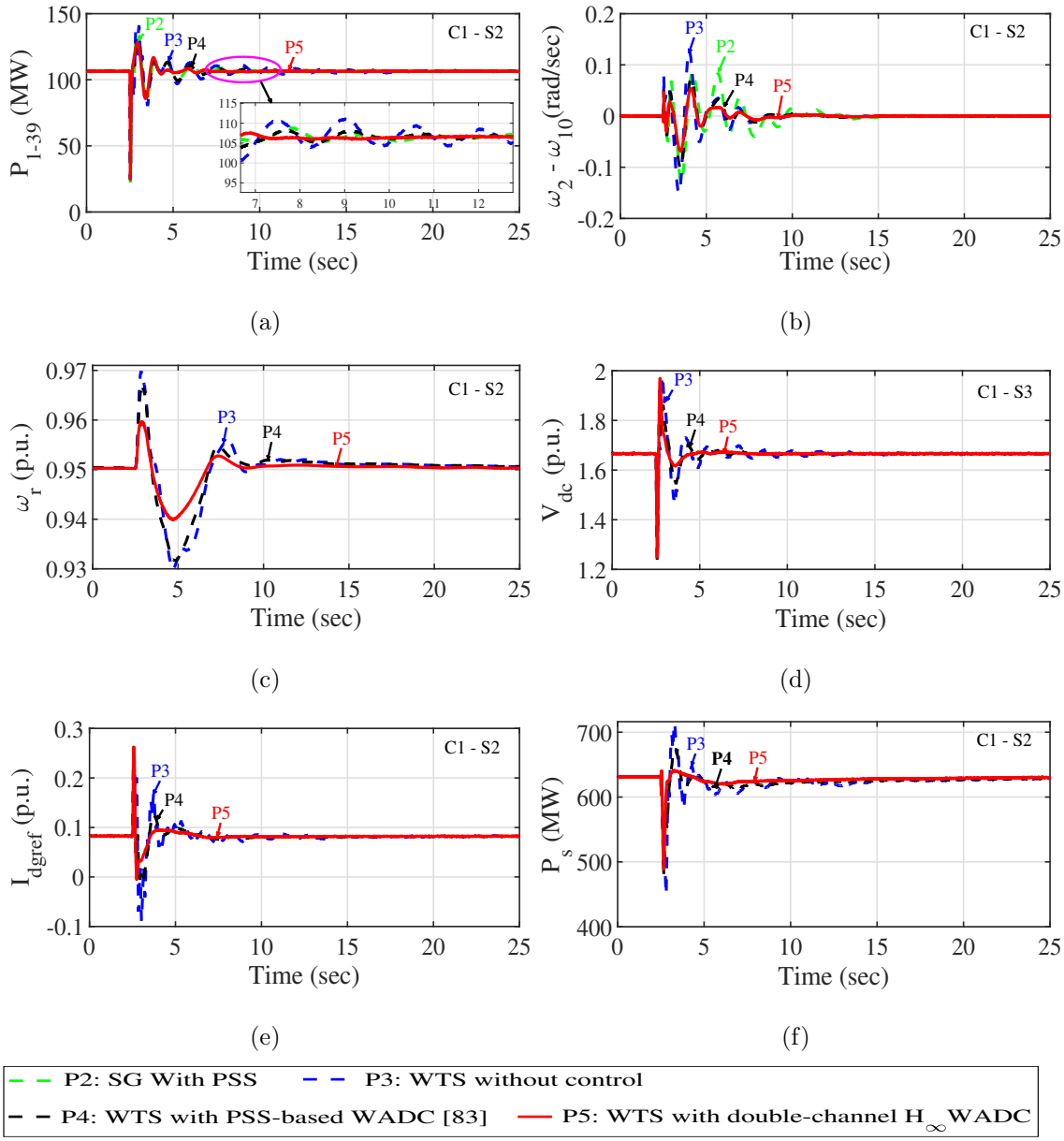

Figure 3.9: Dynamic response of the system with WTS integration in CS4 operating under scenario S2 for contingency C1. (a) Active power of line 1-39, (b) Rotor speed deviation between SG2 and SG10, (c) DFIG rotor speed, (d) DC-link voltage, (e) *d*-axis grid side converter reference current, and (f) WTS active power.

and WTS active power demonstrate effective damping of oscillation magnitude after the imposed contingency C1. These dynamic simulation results reinforce that the proposed WADC exhibits superior damping performance even in severe contingency C1.

Furthermore, to validate the effectiveness of the proposed WADC for WTS, it is simulated under scenario S3. The system's dynamic response is shown in Fig 3.10. Fig 3.10 (a) and (b) illustrate the power flow through line P_{1-39} and the rotor speed difference

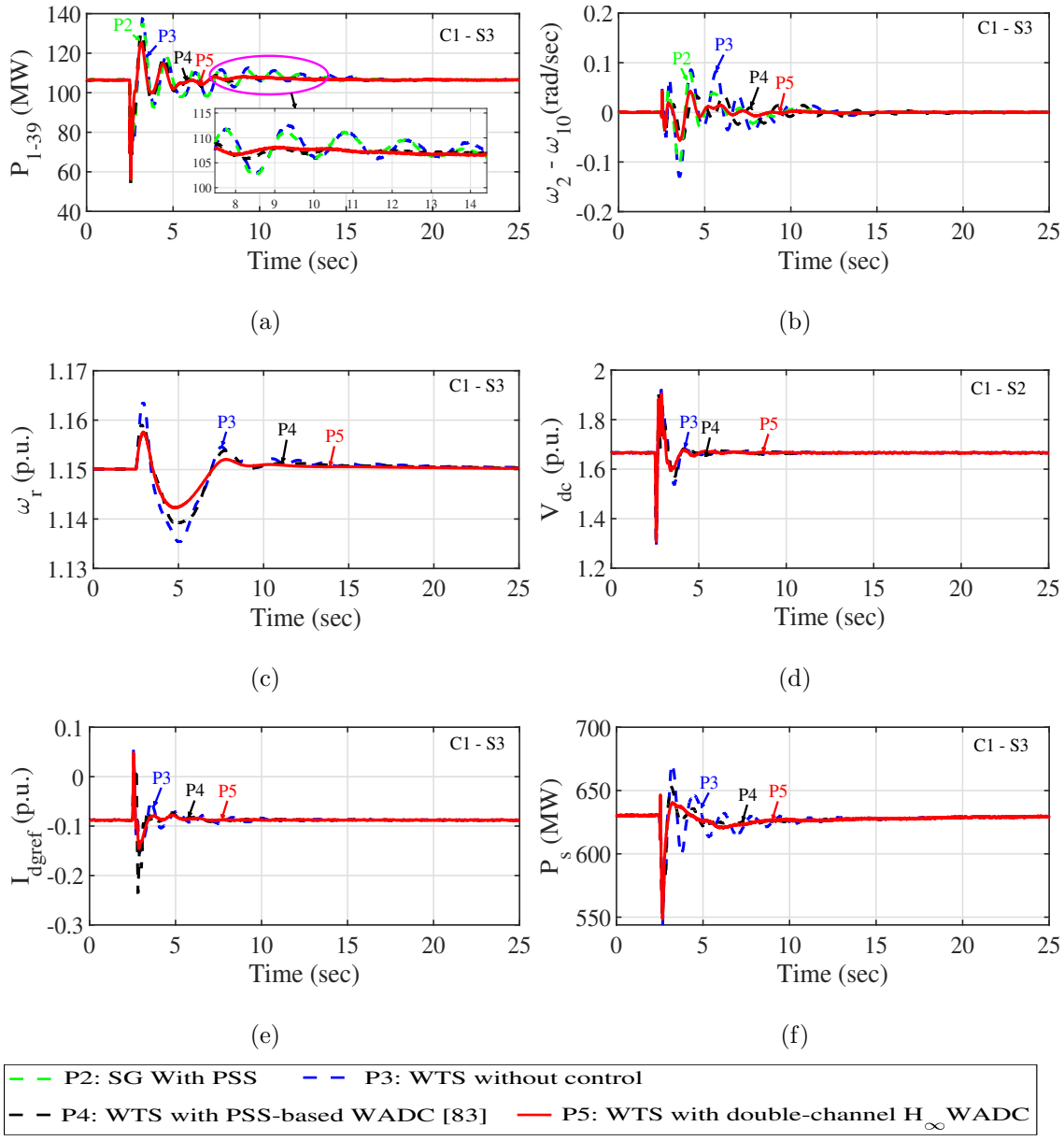

Figure 3.10: Dynamic response of the system with WTS integration in CS4 operating under scenario S3 for contingency C1. (a) Active power of line 1-39, (b) Rotor speed deviation between SG2 and SG10, (c) DFIG rotor speed, (d) DC-link voltage, (e) *d*-axis grid side converter reference current, and (f) WTS active power.

between SG2 and SG10, respectively. This dynamic simulation response shows that the power oscillation and rotor oscillation are significantly reduced compared to PSS-based WADC [83]. When WTS operates in super-synchronous conditions, the DFIG operates at a speed significantly higher than the grid frequency. This results in a reduction of effective inertia, which, in turn, limits the generator's ability to absorb and store energy. The lower effective inertia diminishes its effectiveness in providing damping during system

disturbances. Consequently, when operating in super-synchronous conditions, the proposed WADC system for WTS offers reduced damping capabilities for alleviating power system prominent inter-area oscillations compared to normal and sub-synchronous operation conditions. Also, the damping of oscillations in WTS reactive power, DFIG rotor speed, and DC-link voltage is significantly improved, as illustrated in Fig 3.10 (c) and (d), respectively. Furthermore, the dynamic simulation responses in Fig 3.10 (e) and (f) illustrate the effective damping of oscillations for the d-axis grid side converter reference current and WTS active power, respectively, under operating scenario S3.

From the dynamic simulation responses shown in Fig 3.8, Fig 3.9, and 3.10, it becomes evident that the damping performance of the proposed WADC for WTS is superior when operating under scenario S2 compared to scenarios S1 and S3. Also, the performance of the proposed WADC in mitigating power system dominant inter-area oscillations is better than the PSS-based WADC systems [83].

3.5.2 Contingency 2 (C2)

This analysis simulates the study test system with WTS integrated into CS4 under contingency C2. The dynamic simulation results under operating scenario S2 for power flow across line P_{17-18} and rotor speed deviations between SG2 and SG10 are shown in Fig 3.11(a) and (b), respectively. It's worth noting that the power flow across the line increases due to the permanent outage of the transmission line. Power and rotor speed oscillations are better attenuated compared to the PSS-based WADC [83]. Furthermore, the rotor oscillations' peak overshoot and settling time after the fault are adequately reduced. Furthermore, oscillations in WTS reactive power, DFIG rotor speed, and DC-link voltage following the disturbance are effectively decreased, as illustrated in Fig 3.11 (c) and (d), respectively, for the operating scenario S2. The dynamic simulation responses in Fig. 3.11 (e) and (f) demonstrate a substantial reduction in oscillation for the d-axis reference current of the grid side converter and WTS active power following the imposition of contingency C2. These findings reinforce that the proposed WADC exhibits superior damping performance, even under severe contingency C2 for operating scenario S2.

The dynamic simulation results demonstrate that the proposed double-channel H_∞ WADC provides robust damping performance under reduced system inertia conditions against various contingencies. It also provides robust damping for system-dominant inter-

area oscillations against uncertainties, such as wind speed variations and communication time delays in the feedback control loop.

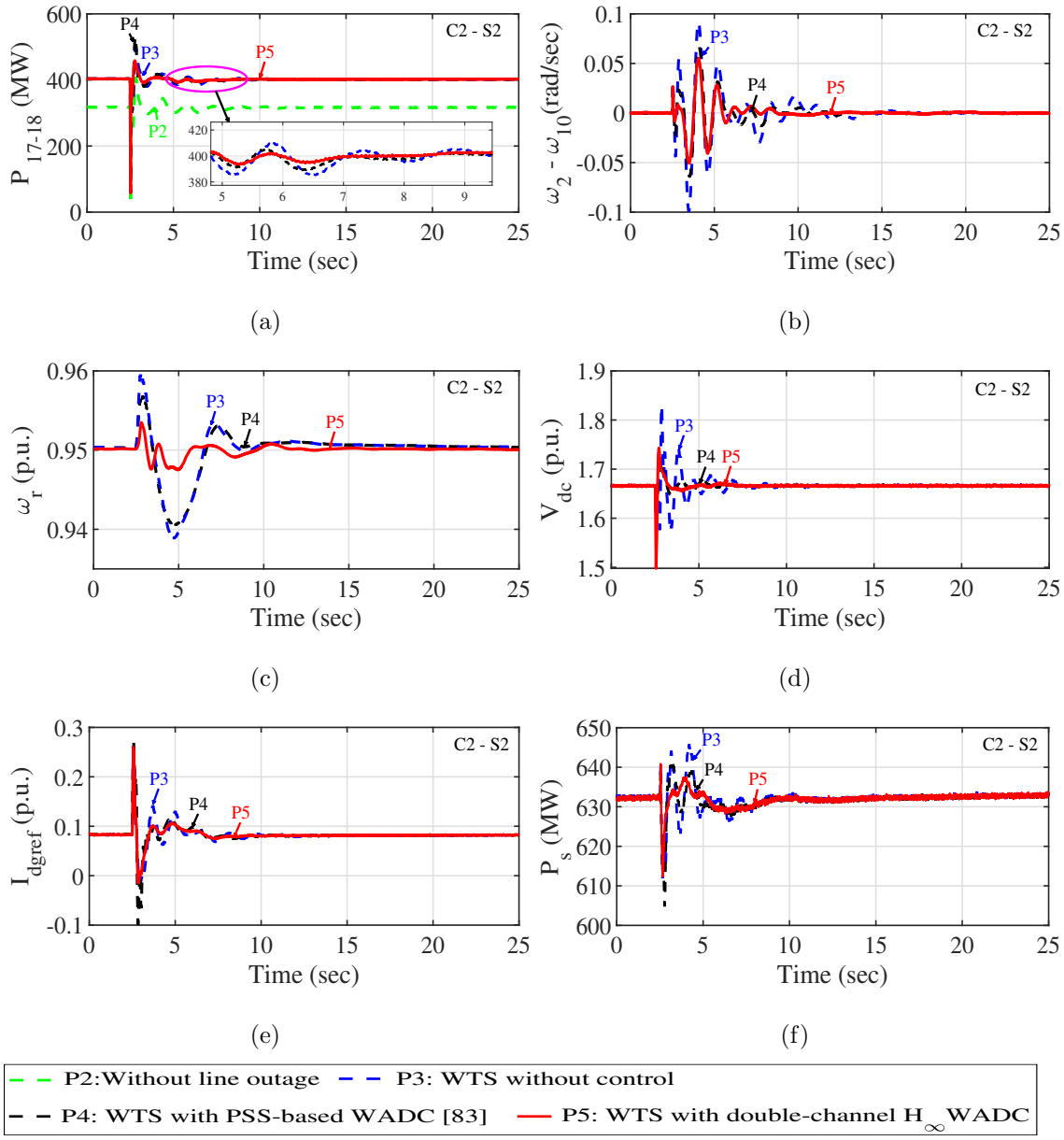

Figure 3.11: Dynamic response of the system with WTS integration in CS4 operating under scenario S2 for contingency C2. (a) Active power of line 1-39, (b) Rotor speed deviation between SG2 and SG10, (c) DFIG rotor speed, (d) DC-link voltage, (e) *d*-axis grid side converter reference current, and (f) WTS active power.

3.6 Summary

In this chapter, a double-channel H_∞ scheme-based WADC was proposed for the WTS integrated power system to enhance the damping of multiple inter-area modes under low system inertia. This study found that the power system inter-area oscillation modes are not only affected by changes in system inertia but also due to close-loop control mode interactions between WTS and SGs under low inertia conditions. Simulations carried out on a practical test system demonstrate the large penetration of WTS leads to considerable deterioration of damping of critical mode of oscillations and introduces unstable oscillation mode that must be eliminated in order to maintain small signal stability of the system. Keeping these aspects in mind, robust WADC was suggested that gives due consideration to dynamic interaction between WTS and rest of the network. Proposed controller was found to be effective not only in damping critical modes of oscillations of WTS integrated power system but also in improving system stability margin. The superiority of the proposed controller was established through a comparative analysis with an existing PSS-based WADC. The proposed WADC was also tested on RTDS platform to assess its feasibility in a real-time environment. The results obtained through modal analysis and dynamic simulation affirm the efficacy and superiority of the proposed WADC over an existing PSS-based WADC.